

# Growth and device processing of hexagonal boron nitride epilayers for thermal neutron and deep ultraviolet detectors

T. C. Doan, J. Li, J. Y. Lin, and H. X. Jiang<sup>a</sup>

*Department of Electrical & Computer Engineering, Texas Tech University,  
Lubbock, TX 79409, USA*

(Received 3 February 2016; accepted 12 July 2016; published online 26 July 2016)

Solid-state neutron detectors with high performance are highly sought after for the detection of fissile materials. However, direct-conversion neutron detectors based on semiconductors with a measureable efficiency have not been realized. We report here the first successful demonstration of a direct-conversion semiconductor neutron detector with an overall detection efficiency for thermal neutrons of 4% and a charge collection efficiency as high as 83%. The detector is based on a 2.7  $\mu\text{m}$  thick  $^{10}\text{B}$ -enriched hexagonal boron nitride (*h*-BN) epitaxial layer. The results represent a significant step towards the realization of practical neutron detectors based on *h*-BN epilayers. Neutron detectors based on *h*-BN are expected to possess all the advantages of semiconductor devices including wafer-scale processing, compact size, light weight, and ability to integrate with other functional devices. © 2016 Author(s). All article content, except where otherwise noted, is licensed under a Creative Commons Attribution (CC BY) license (<http://creativecommons.org/licenses/by/4.0/>). [<http://dx.doi.org/10.1063/1.4959595>]

## I. INTRODUCTION

Among the members of the III-nitrides, hexagonal boron nitride (*h*-BN) is the least studied and understood. Its extraordinary physical properties make *h*-BN highly promising for emerging device applications. With an energy bandgap around 6.5 eV, *h*-BN has become as an important semiconductor material.<sup>1–7</sup> With its high temperature and chemical stability, *h*-BN has potential applications in high temperature/power electronic device applications. P-type conductivity seems to be more easily to realize in *h*-BN than in AlN, which reveals the potential of *h*-BN for deep UV emitter and detector applications.<sup>6,7</sup> With its close lattice match to graphene and relatively chemically inert surface, *h*-BN is the most suitable substrate/dielectric/separation layer for the realization of van der Waals heterostructure devices.<sup>8</sup> With the large thermal neutron cross-section of B-10 ( $^{10}\text{B}$ ) isotope ( $\sim 3840$  barns),<sup>9</sup> *h*-BN is also a promising material for realizing solid-state neutron detectors.<sup>10–12</sup> The development of solid-state neutron detection technologies that do not require the use of  $^3\text{He}$  gas will not only enable the researchers and users to dedicate the scarce supplies of  $^3\text{He}$  gas to other applications for which no substitutes are possible, but also opens up new applications ranging from fissile materials sensing, neutron therapy, medical imaging, probing of crystal structures, to oil exploration.

However, active devices such as deep UV emitters and photodetectors and thermal neutron detectors based on *h*-BN with measureable efficiencies have not been realized due to the fact that *h*-BN materials are still at an early development stage. Thermal neutron detectors based on *h*-BN so far were fabricated from thin natural *h*-BN epilayers,<sup>10–12</sup> in which the element B consists of approximately 20% of  $^{10}\text{B}$  and 80% of  $^{11}\text{B}$ , respectively.<sup>9,13</sup> Due to the relatively large absorption length of thermal neutrons (with a kinetic energy of 25 meV) of 237  $\mu\text{m}$  in natural *h*-BN,<sup>10,11,14</sup>

<sup>a</sup>Email: [hx.jiang@ttu.edu](mailto:hx.jiang@ttu.edu)



the use of such thin natural *h*-BN layers in the neutron detectors provides a negligibly small thermal neutron absorption, which limited the ability to evaluate the charge collection as well as the overall detection efficiency. One of the most effective approaches to increase the neutron detection efficiency is by  $^{10}\text{B}$  isotopic enrichment of the source molecule, which would increase the thermal neutron absorption efficiency and reduce the thermal neutron absorption length by a factor 5 with little impact on the semiconducting properties. For  $^{10}\text{B}$ -enriched *h*-BN epilayers (with 100%  $^{10}\text{B}$  isotopic enrichment), the thermal neutron absorption length is reduced to 47  $\mu\text{m}$  in comparison to 237  $\mu\text{m}$  for natural *h*-BN.<sup>11</sup> In this work, we report on the successful growth of natural *h*-BN epilayers with a thickness of 4.5  $\mu\text{m}$  and  $^{10}\text{B}$ -enriched *h*-BN epilayers with a thickness of 2.7  $\mu\text{m}$ . Neutron detectors fabricated from  $^{10}\text{B}$ -enriched *h*-BN (*h*- $^{10}\text{B}\text{N}$ ) epilayers with a thickness of 2.7  $\mu\text{m}$  were shown to exhibit a 4% detection efficiency for thermal neutrons and a charge collection efficiency as high as 83%. The results represent a significant step towards the realization of practical direct-conversion neutron detectors based *h*-BN epilayers.

## II. EXPERIMENT

Epitaxial layers of *h*-BN were grown by metal organic chemical vapor deposition (MOCVD) on *c*-plane sapphire substrates. The layer structure is schematically shown in Fig. 1(a). The precursors for boron and nitrogen were trimethylboron (TMB) and  $\text{NH}_3$  were used as boron and nitrogen precursors, respectively. Hydrogen was used as a carrier gas. A pulsed growth scheme (alternating flows of TMB and  $\text{NH}_3$ ) previously developed for  $\text{AlN}$ <sup>15-17</sup> was adopted to minimize the pre-reaction between TMB and  $\text{NH}_3$ , which is important for obtaining epilayers with low defect density. As in the case of GaN and AlN epilayers,<sup>18</sup> due to the lattice mismatch between *h*-BN and  $\text{Al}_2\text{O}_3$ , a low temperature BN buffer layer of about 10 nm in thickness was deposited at  $\sim 800^\circ\text{C}$  on the sapphire substrate prior to the growth of *h*-BN epilayer. This buffer serves as a nucleation layer and also enhances the adhesion of the subsequent *h*-BN epilayer. The growth temperature and

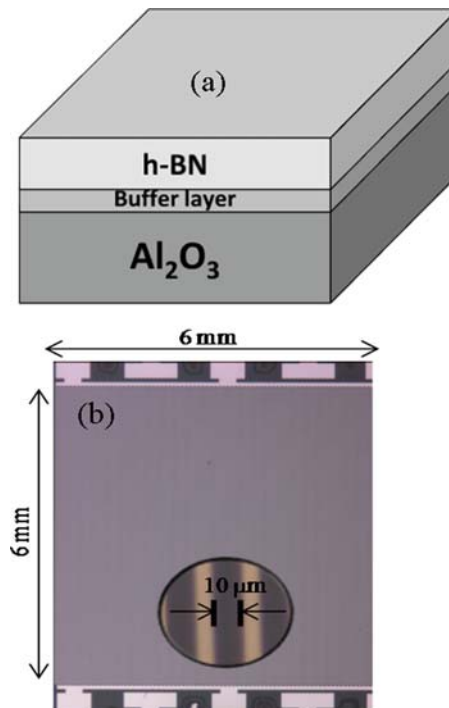


FIG. 1. (a) Schematic layer structure of *h*-BN epilayers used for neutron detector fabrication. (b) Optical image of a fabricated metal-semiconductor-metal (MSM) detector incorporating a natural *h*-BN epilayer with a thickness of 4.5  $\mu\text{m}$ . The device size is 6 mm x 6 mm having the widths of etched trenches and micro-strips of 10  $\mu\text{m}$  and 10  $\mu\text{m}$ , respectively.

pressure for the subsequent *h*-BN epilayers were about 1350 °C and ~100 torr respectively. One of the significant progresses made recently in the growth of *h*-BN epilayers is the identification of the nitrogen vacancy ( $V_N$ ) related point defects as the origin of the deep level defects which act as charge carrier traps.<sup>19</sup> Thus the growth was carried out in N-rich conditions with a typical V/III ratio of around 3000 to minimizing the density of  $V_N$  and  $V_N$  related point defects.

Detectors based on a metal-semiconductor-metal (MSM) architecture with micro-strip interdigital fingers were fabricated from *h*-BN epilayers by adopting the basic device processes developed for GaN<sup>20</sup> to take advantage of the excellent lateral transport properties of *h*-BN epilayers. The photolithography technique was used to pattern the interdigital fingers on the surface of *h*-BN epilayers. Pattern transfer was accomplished using a sulfur hexafluoride ( $SF_6$ ) gas-based inductively-coupled plasma (ICP) dry etching.<sup>21,22</sup> The patterns were etched all the way to the sapphire substrate. Metal contacts consisting of bi-layers of Ti/Al (20nm/30nm) were deposited by e-beam evaporation.

### III. RESULTS AND DISCUSSION

#### A. Natural *h*-BN detector

Figure 1(b) is a micrograph of a representative MSM detector fabricated from a natural *h*-BN epilayer with a thickness of 4.5  $\mu\text{m}$  and having a device area of 6 mm x 6 mm and the widths of etched trenches and micro-strips of 10  $\mu\text{m}$  and 10  $\mu\text{m}$ , respectively. Owing to its wide bandgap, undoped *h*-BN epilayers are highly insulating. As such, *h*-BN detectors exhibit extremely small leakage current density. This is illustrated in Fig. 2(a), where the dark I-V characteristic (leakage current density vs. applied bias voltage) of a fabricated detector is shown. For instance, at a typical operating voltage of 10 V, the leakage current density is below  $10^{-11}$  A/cm<sup>2</sup>, which is about 5 orders of magnitude lower than that of the state-of-the-art boron filled micro-structured Si detectors.<sup>23</sup> A representative photo-spectral response of an *h*-BN photodetector is shown in Fig. 2(b). The *h*-BN MSM photodetectors exhibit a peak response at 217 nm and a sharp cut-off wavelength around 230 nm with virtually no detectable responses in the long wavelengths. These results indicate that *h*-BN MSM devices performed well as a deep UV photodetector.

Another very important parameter that characterizes the electronic quality of a semiconductor for detector fabrication is its charge carrier mobility-lifetime ( $\mu\tau$ ) product. The  $\mu\tau$  product determines the drift length of the excess free carriers per unit electric field (E) before recombination or trapping occurs. To ensure a charge collection under an applied electric field (E), the drift length ( $=\mu\tau E$ ) of the electrons and holes under an applied electric field must be greater than the spacing between the electrodes (L). This means that the minimum acceptable  $\mu\tau$  product is  $\mu\tau \geq \frac{L}{E}$  (cm<sup>2</sup>/V). Increasing the  $\mu\tau$  product ultimately will enhance the charge collection efficiency and hence the performance of the fabricated detector. This parameter is significantly influenced by the presence of impurities/defects (which act as charge carrier traps) introduced during the crystal growth and device processing. To characterize the mobility and lifetime product ( $\mu\tau$ ), I-V characteristics of the MSM detectors under light illumination were measured. Photo-excited electrons and holes are drifted to the electrodes under an applied electric field. The I-V characteristics are described by a modified Many's equation for lateral transport:<sup>24,25</sup>

$$I(V) = I_0 \left[ \frac{\mu_e \tau_e V}{L^2} - \left( \frac{\mu_e \tau_e V}{L^2} \right)^2 \left( 1 - e^{-\frac{L^2}{\mu_e \tau_e V}} \right) + \frac{\mu_h \tau_h V}{L^2} - \left( \frac{\mu_h \tau_h V}{L^2} \right)^2 \left( 1 - e^{-\frac{L^2}{\mu_h \tau_h V}} \right) \right], \quad (1)$$

where V is the applied bias voltage and L is the spacing between the electrodes,  $\mu_e \tau_e$  and  $\mu_h \tau_h$  are the mobility-lifetime products of electrons and holes, respectively, and  $I_0$  is the saturation current.

It is reasonable to assume that  $\mu_e \tau_e = \mu_h \tau_h = \mu\tau$  for *h*-BN epilayers in the lateral direction based on the fact that the electrons and holes have an identical dispersion and effective mass in single sheet *h*-BN.<sup>26–28</sup> As such, Eq. (1) reduces to

$$I(V) = 2I_0 \left[ \frac{V}{W} - \left( \frac{V}{W} \right)^2 \left( 1 - e^{-\frac{W}{V}} \right) \right], \quad (2)$$

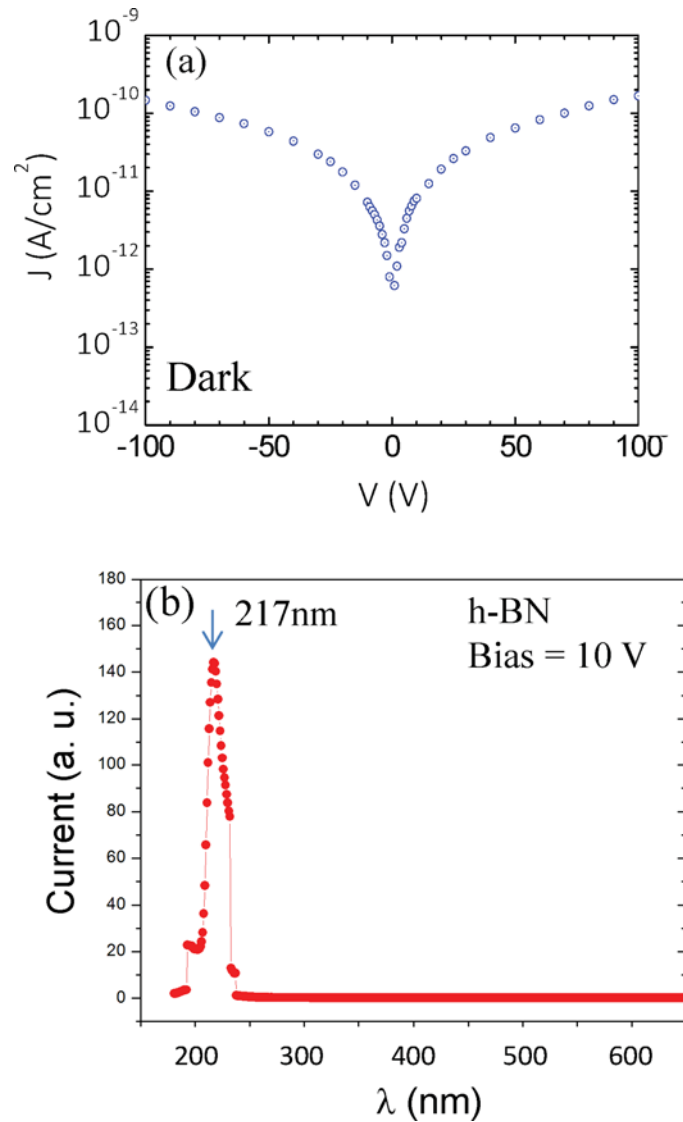


FIG. 2. (a) Dark I-V characteristic (leakage current density vs. applied bias voltage) of an *h*-BN MSM detector. (b) The relative photo-spectral response of an *h*-BN MSM photodetector measured at a bias voltage of 10 V.

where  $W = \frac{L^2}{\mu\tau}$ . It is clear from Eq. (2) that in the absence of an external applied bias voltage (or electrical field), there is no charge collection and the photocurrent  $I(0) = 0$ . As the external applied bias voltage increases, the asymptotic form of the bracket in Eq. (2) approaches to  $\frac{1}{2}$  and the photocurrent approaches to the saturation value of  $2I_0 \times \frac{1}{2} = I_0$  at very large values of  $V$ . Figure 3 plots the measured I-V characteristics under light illumination for a detector incorporating a layer of *h*-BN of 4.5  $\mu\text{m}$  in thickness. In Fig. 3, the solid curve is a least squares fit of experimental data (open squares) with Eq. (2), from which we obtain the fitted value of  $\mu\tau$  of  $0.54 \times 10^{-7} \text{ cm}^2/\text{V}$  for 4.5  $\mu\text{m}$  thick *h*-BN epilayers. To ensure a charge collection, the minimum required external applied electrical field is  $E_{\text{min}} = \frac{L}{\mu\tau} = \frac{10 \mu\text{m}}{\mu\tau}$ . With  $\mu\tau = 0.54 \times 10^{-7} \text{ cm}^2/\text{V}$ ,  $E_{\text{min}} \approx 2 \times 10^4 \text{ V/cm}$ . This translates to a minimum bias voltage of 20 V that must be applied between the electrodes to ensure an adequate charge collection in the detector.

To characterize the thermal neutron response, we have constructed a neutron source system and associated electronics for measuring the pulse height spectra of the reaction products. The experimental geometry and HDPE size and thickness are identical to those described in the thesis of J. Clinton<sup>29</sup> and based on a depleted sealed source model 100 californium-252 source (<sup>252</sup>Cf)

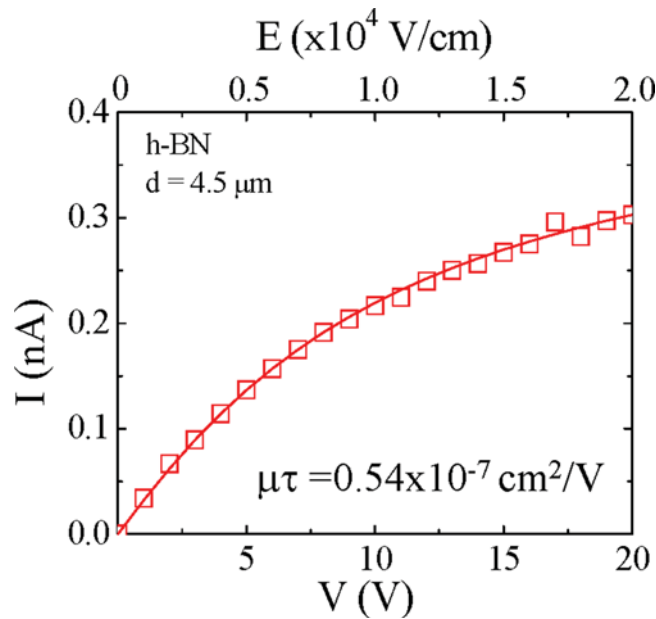


FIG. 3. I-V characteristics of an *h*-BN detector (4.5 μm thick) under light illumination by a broad band spectrum light source (LDLS, EQ-99 by Energetiq). Open squares are the measured data and solid line is the least squares fit of data with a modified Many's equation for lateral transport shown in Eq. (2), from which we obtain the fitted value of  $\mu\tau$ . The size of the squares indicates the error bar size of the data points.

which contained 4.2 μg of active <sup>252</sup>Cf from Frontier Technology, moderated by a high density polyethylene block (HDPE). The <sup>252</sup>Cf source has a half-life of 2.645 years and emits spontaneous fission neutrons with an energy spectrum that follows approximately a Watt distribution with an emission peak at ~0.7 MeV.<sup>30,31</sup> At the time of shipment, the specified neutron intensity was ~1x10<sup>7</sup> neutrons/second based on the mass of active <sup>252</sup>Cf, half-life, fission probability and the number of neutrons per fission. The measurement of thermal neutron responses of *h*-BN detectors was performed 515 days after the source shipment. Based on the known half-life of  $t_{1/2}=2.645$  years,<sup>30,31</sup> the neutron intensity of <sup>252</sup>Cf source on the day of this experimental measurement,  $N(t)$ , can be calculated according to  $N(t)=N_0\text{Exp}(-t/\tau)$ , where  $\tau=t_{1/2}/\ln 2$ ,  $t_{1/2}=2.645 \times 365$  days,  $N_0=1 \times 10^7$ ,  $t=515$  days, providing  $N(t)=7 \times 10^6$  neutrons/second. The HDPE housing was fabricated with two purposes in mind, to act as a safe storage vessel for the <sup>252</sup>Cf source and to perform the moderation of the emitted fast neutrons to obtain a source of thermal neutrons. As schematically illustrated in Fig. 4(a), if the neutron source is placed at the position “A”, most fast neutrons are stopped by the HDPE moderator. If the neutron source is placed at the position “B” which is 2.54 cm to the front surface of the HDPE moderator, neutrons emerging from the front surface are mostly thermal neutrons (neutrons with a kinetic energy ranging from 1 to 100 meV with a spectral peak at 25 meV). The size of this moderator was chosen such that neutrons would exit only from the front face of the HDPE housing during device exposure. These details ensured that lab safety would be maintained throughout the lifetime of this source. Raw thermal neutron count rates were taken from an un-moderated <sup>3</sup>He rate meter at varying distances and the results revealed that the thermal neutron counts are inversely proportional to the distance to the <sup>252</sup>Cf source,  $d$ .<sup>11</sup> This means that the point source model can be appropriately applied to calculate the thermal neutron flux ( $\Phi$ ) ratio at two different distances,  $\frac{\Phi_2}{\Phi_1} = \frac{d_1^2}{d_2^2}$ .

For the reaction product pulse height spectra measurements, the <sup>252</sup>Cf source was placed at position B and detectors were placed a distance of 9 cm to the moderator's front surface. Monte Carlo N particle code simulations, which modeled the interactions of neutrons with hydrogen atoms in the HDPE moderator, provide a conversion ratio of  $2.43 \times 10^{-4}$  for the neutron flux from the <sup>252</sup>Cf source (placed at the position B inside the HDPE moderator) to thermal neutrons at a point in the

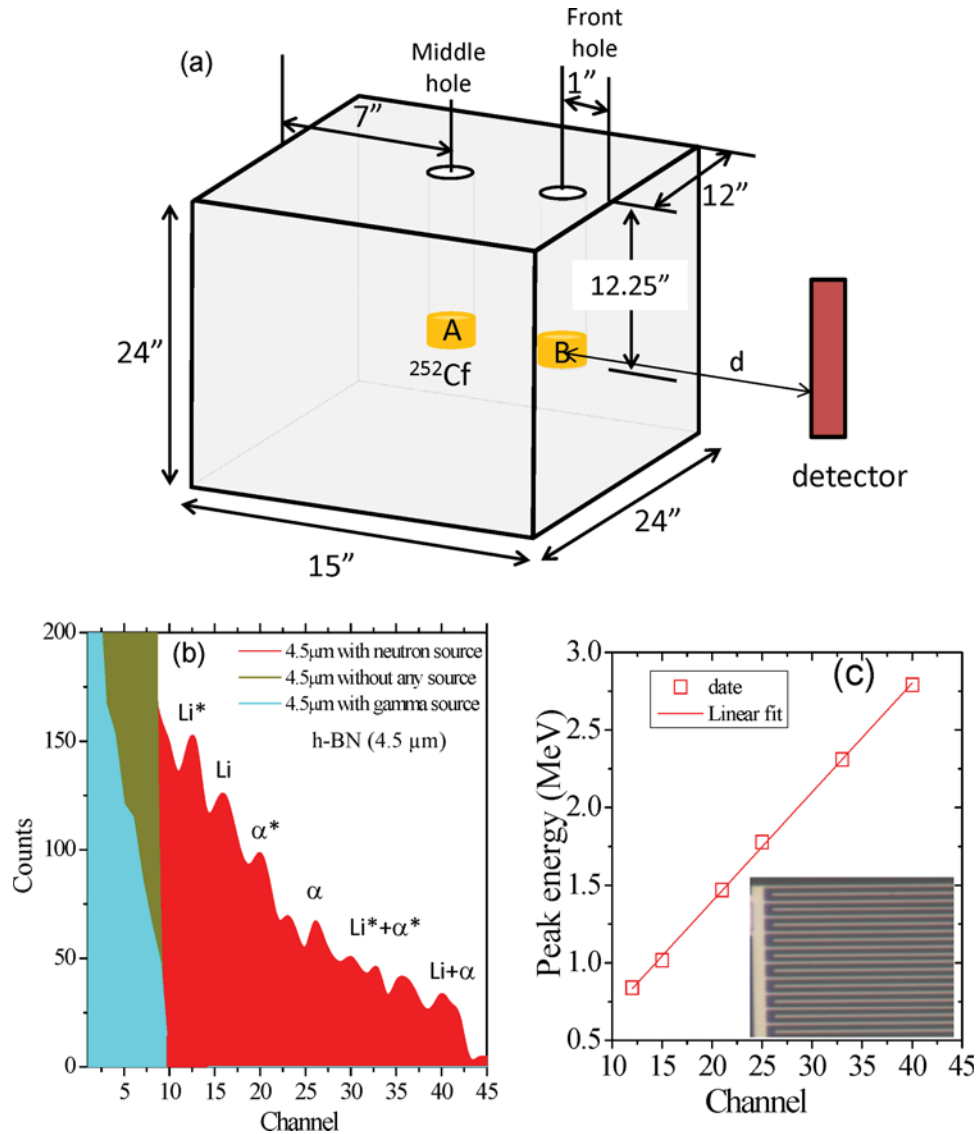


FIG. 4. (a) Schematic diagram of thermal neutron source consisting of a  $^{252}\text{Cf}$  source moderated by a high density polyethylene (HDPE) moderator. The distance  $d$  is measured to the  $^{252}\text{Cf}$  source (inside of the HDPE moderator at the position B). (b) Nuclear reaction pulse height spectrum (counts versus channel number) obtained by a detector incorporating natural  $h\text{-BN}$  of  $4.5\ \mu\text{m}$  in thickness with a counting time of 20 minutes. The detector has a dimension of  $36\ \text{mm}^2$  ( $6\ \text{mm} \times 6\ \text{mm}$ ) and the widths of etched trenches and micro-strips of  $10\ \mu\text{m}$  and  $10\ \mu\text{m}$ , respectively. The dark yellow and red column bars are the total counts measured in the absence and in the presence of the  $^{252}\text{Cf}$  source, respectively. The blue-green column bars represent the measured counts while the detector is irradiated by a  $\gamma$ -photon source produced by  $^{137}\text{Cs}$  decay only. (c) Energy peak calibration among the nuclear reaction products expected from Eq. (4). The open squares in Fig. 4(c) are the data points and the solid line is a linear fit. The inset of Fig. 4(c) is an expanded view of an MSM device having the widths of etched trenches/micro-strips of  $10\ \mu\text{m}/10\ \mu\text{m}$  showing the edge effect due to the specific arrangement of the interdigital finger metal contacts.

air that is 10 cm away from the moderator's front surface.<sup>29</sup> Using the point source model, the flux of the thermal neutrons at 9 cm away from the front surface of the HDPE moderator can thus be calculated according to  $7 \times 10^6 \times 2.43 \times 10^{-4} \frac{(10 + 2.54)^2}{(9 + 2.54)^2} = 2 \times 10^3$  (thermal neutron/cm<sup>2</sup> · s). The detector was bonded in a ten pin ceramic flat pack and placed inside a metal box to reduce the electronic noise and connected to a charge sensitive modified preamplifier (Cremat, Inc.). The pulse-height spectra were measured with a multi-channel analyzer (MCA) (model 8000D by Amptek). The

pulse-height spectra of the nuclear reaction product were measured for a total counting time of 1200 s for detectors incorporating a 4.5  $\mu\text{m}$  thick *h*-BN epilayer.

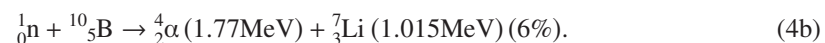
The measured pulse-height spectrum of a 4.5  $\mu\text{m}$  thick detector is shown in Fig. 4(b). The dark yellow column bars in Fig. 4(b) are the background counts or the total counts measured in the absence of the  $^{252}\text{Cf}$  source. The red column bars in Fig. 4(b) are the total counts measured in the presence of the  $^{252}\text{Cf}$  source and the blue-green column bars represent the measured counts while the detector was irradiated by a  $\gamma$ -ray source produced by  $^{137}\text{Cs}$  decay only. In the absence of any radiation sources, the counts are just background noise and no counts were observed beyond channel 13. Moreover, as seen from Fig. 4(b), the *h*-BN detector has a negligible response to  $\gamma$ -photons produced by  $^{137}\text{Cs}$  decay with an energy at 0.662 MeV, i.e., the counts were below the background noise under the irradiation of  $\gamma$ -photons. This fact is expected because BN is composed of low atomic number elements and so BN's interaction with  $\gamma$  photons should be low. Under irradiation of thermal neutrons, the total number of thermal neutrons irradiating on the detector (with a device area of  $A = 0.6 \times 0.6 = 0.36 \text{ cm}^2$ ) during the 1200 s counting time is  $N_{\text{in}} = \Phi A \cdot (\text{counting time}) = 2 \times 10^3 \times 0.36 \times 1200 = 8.6 \times 10^5$ , whereas the measured counts in response to the thermal neutron source ( $^{252}\text{Cf}$  source placed at the position B inside the HPDE moderator) is  $N_c = 5.5 \times 10^3$ . This gives an overall detection efficiency of  $\eta = \frac{N_c}{N_{\text{in}}} \approx 0.64\%$  for 4.5  $\mu\text{m}$  thick natural *h*-BN detectors.

To compare the measured detection efficiency with expectation, we consider the interaction probability as a function of the *h*-BN detector layer thickness. The probability of interaction (P) between the thermal neutrons and *h*-BN epilayers follows

$$P = 1 - \exp\left(-\frac{t}{\lambda}\right), \quad (3)$$

where  $\lambda$  is the thermal neutron absorption length of *h*-BN ( $=237 \mu\text{m}$  for natural *h*-BN and  $=47 \mu\text{m}$  for  $^{10}\text{h}$ -BN) and  $t$  is the *h*-BN epilayer thickness. Equation (3) indicates that for thin epilayers ( $t \ll \lambda$ ), the interaction probability increases linearly with the layer thickness ( $t$ ),  $p \approx \frac{t}{\lambda}$ . Thus the expected maximum detection efficiency of a detector incorporating a layer thickness of 4.5  $\mu\text{m}$  natural *h*-BN is  $p_{\text{max}} \approx \frac{t}{\lambda} \times 0.5 = \frac{4.5}{237} \times 0.5 = 0.95\%$ , where a fraction of 0.5 is include in the calculation to account for the fact that half of the *h*-BN detection area was etched away for this device. The discrepancy between the measured and the expected maximum efficiency (or the interaction probability) can be accounted for by the charge collection efficiency. The charge collection efficiency ( $\eta_{\text{coll}}$ ) is one of the most important parameters of a radiation detector and knowing this parameter is highly useful to the further development of *h*-BN materials and devices since this parameter depends on the overall material and device quality. This parameter is defined as the ratio of the measured detection efficiency ( $\eta$ ) to the interaction probability (P) according to  $\eta_{\text{coll}} = \frac{\eta}{P} = \frac{0.64}{0.95}$ . The result reveals that the charge collection efficiency of *h*-BN detectors is about 67%. This relatively high charge collection efficiency is a result of the single crystalline nature of *h*-BN. However, the overall detection efficiency ( $\eta$ ) of this batch of *h*-BN detectors is below 1% because the devices incorporate natural *h*-BN epilayers with a thickness less than 5  $\mu\text{m}$  and 50% of the detection area was removed by dry etching in the MSM detector design shown in Fig. 1(b).

One of the interesting features of the *h*-BN thin film detectors is their ability to resolve the reaction products.<sup>11,12</sup> The measured pulse-height spectrum of the 4.5  $\mu\text{m}$  thick detector shown in Fig. 4(b) exhibits well resolved peaks corresponding to the product energies of  $^{10}\text{B}$  and thermal neutron reaction described by<sup>9</sup>



These include  $\text{Li}^*$ ,  $\text{Li}$ ,  $\alpha^*$  and  $\alpha$  peaks as well as the sum peaks of  $\text{Li}^* + \alpha^*$  (2.31 MeV) and  $\text{Li} + \alpha$  (2.785 MeV). The calibration between the energy and channel number for the whole spectrum of the 4.5  $\mu\text{m}$  thick detector is plotted in Fig. 4(c), which shows a linear relationship between the reaction product energies of  $\text{Li}^*$ ,  $\text{Li}$ ,  $\alpha^*$ ,  $\alpha$ ,  $\text{Li}^* + \alpha^*$ , and  $\text{Li} + \alpha$  peaks and the channel numbers, exactly corresponding to the values expected from Eq. (4). The good agreement between the experimental data and expected energy peaks/peak separations of the nuclear reaction products shown in Fig. 4(c)

provides an assurance in our assignment of the observed peaks in the pulse-height spectrum. There are several unidentified peaks in Fig. 4(b) in addition to those expected from the reaction product energies of Eq. (4), which are most likely due to the edge effect, i.e., the electrical field is not uniform across the entire MSM detector surface because of the specific arrangement of the metal contacts in the interdigital finger format. The inset of Fig. 4(c) is an expanded optical image view of an MSM detector edge showing the widths of etched trenches/micro-strips of  $10\ \mu\text{m}/10\ \mu\text{m}$ . By more carefully inspecting how a metal finger contact is inserted in between two other fingers, one can see that the electrical field near the detector edge can be slightly lower than that in the center, leading to additional peaks in the pulse-height spectrum.

## B. $^{10}\text{B}$ isotopically enriched $h\text{-BN}$ detectors

In Figure 5, we plot the results of Eq. (3) for both natural  $h\text{-BN}$  and  $^{10}h\text{-BN}$  layers, which represent the upper limit of the detection efficiency values (or the interaction probabilities) of  $h\text{-BN}$  and  $^{10}h\text{-BN}$  detectors. The results clearly indicate that the use of  $^{10}h\text{-BN}$  epilayers will significantly enhance the interaction probability and hence the thermal neutron detection efficiency. The  $^{10}h\text{-BN}$  MSM detectors were fabricated using the same device processing procedures as for  $h\text{-BN}$  detectors with the exception that  $^{10}h\text{-BN}$  MSM detectors have a  $^{10}h\text{-BN}$  layer thickness of  $2.7\ \mu\text{m}$ , device area of  $5\ \text{mm} \times 5\ \text{mm}$ , and the micro-strip width of  $15\ \mu\text{m}$  and etched trench width of  $3\ \mu\text{m}$ . This design reduces the fraction of removed  $^{10}h\text{-BN}$  materials and increases the detection area, as illustrated in Fig. 6(a). Figure 6(b) shows a typical pulse height spectrum of the thermal neutron and  $^{10}\text{B}$  reaction products measured by a  $^{10}h\text{-BN}$  detector using the same procedures as those described for natural  $h\text{-BN}$  detectors except that the counting time was reduced to 600 s. This gives  $N_{\text{in}} = \Phi A \cdot (\text{counting time}) = 2 \times 10^3 \times 0.25\ \text{cm}^2 \times 600\ \text{s} = 3 \times 10^5$ . Similar to those of natural  $h\text{-BN}$  detectors,  $^{10}h\text{-BN}$  detector has a negligible response to  $\gamma$  photons produced by  $^{137}\text{Cs}$  decay with an energy at 0.662 MeV. Due to  $^{10}\text{B}$  isotopic enrichment and hence an enhancement in the interaction probability, the sum peak at 2.31 MeV is the most predominant in the pulse height spectrum. The absence of the 2.79 MeV sum peak is mostly likely due to the fact that the range of the 1.77 MeV  $\alpha$  particles ( $\sim 4.6\ \mu\text{m}$ )<sup>32</sup> is larger than the  $^{10}h\text{-BN}$  detector thickness ( $2.7\ \mu\text{m}$ ) and the lower nuclear reaction probability (6% for the 2.79 MeV sum peak vs 94% for the 2.31 MeV sum peak). The overall detection efficiency ( $\eta$ ) of  $^{10}h\text{-BN}$  detectors (with a layer thickness of  $2.7\ \mu\text{m}$ ) can also be determined from the ratio of the measured counts in response to the thermal neutrons ( $N_{\text{c}}$ ) to the total number of thermal neutrons irradiating on the detector ( $N_{\text{in}}$ ). Since our  $^{10}h\text{-BN}$  wafers

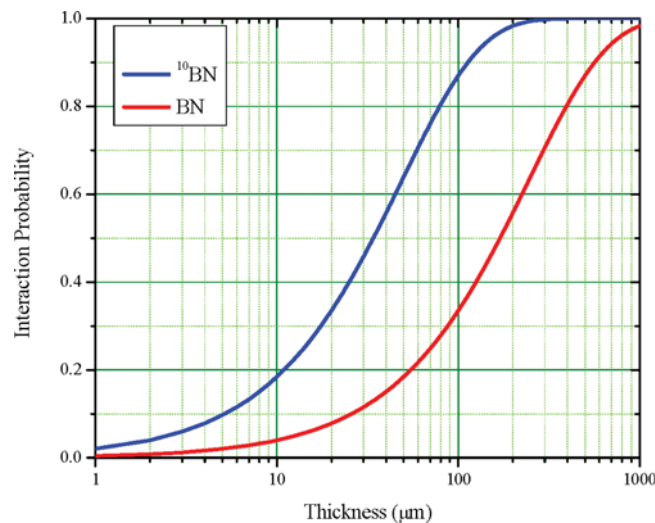


FIG. 5. Plot of Eq. (3), the probability of interaction ( $P$ ) between the thermal neutrons and  $h\text{-BN}$  epilayers,  $P = 1 - \exp(-\frac{t}{\lambda})$ , as a function of the layer thickness for both natural and  $^{10}\text{B}$ -enriched  $h\text{-BN}$ .

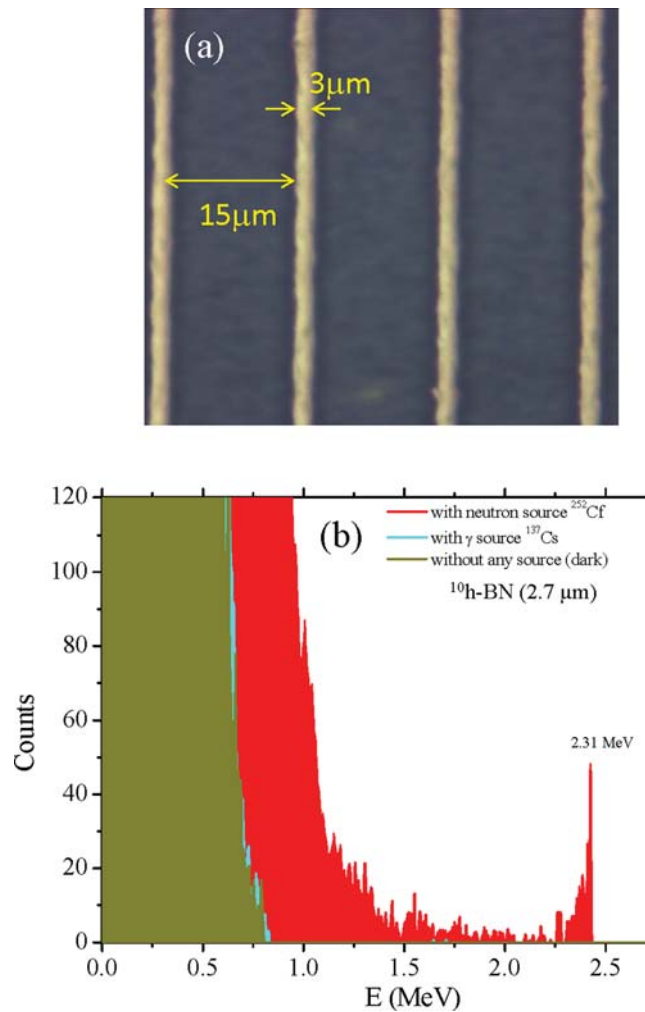


FIG. 6. (a) Optical image of a portion of a detector fabricated from isotopically  $^{10}\text{B}$ -enriched  $h\text{-BN}$  epilayer ( $^{10}h\text{-BN}$ ) of  $2.7\ \mu\text{m}$  in thickness. The detector has a dimension of  $25\ \text{mm}^2$  ( $5\ \text{mm} \times 5\ \text{mm}$ ) and the widths of etched trenches and micro-strips of  $3\ \mu\text{m}$  and  $15\ \mu\text{m}$ , respectively. (b) Nuclear reaction pulse height spectrum measured by a  $^{10}h\text{-BN}$  detector using the same thermal neutron source setup shown in Fig. 4(a). The counting time is 10 minutes. The dark yellow and red column bars are the total counts measured in the absence and in the presence of the  $^{252}\text{Cf}$  source, respectively. The blue-green column bars represent the measured counts while the detector was only irradiated by a  $\gamma$ -photon source produced by  $^{137}\text{Cs}$  decay.

are 4-inches in diameter, our device fabrication undergoes wafer scale processing, which allows us to produce multiple nearly identical detectors for characterization. By averaging over a multiple measurements, we obtain  $N_c = 1.2 (\pm 0.03) \times 10^4$ . This provides an overall detection efficiency of  $\eta = \frac{N_c}{N_{\text{in}}} = 4.0 (\pm 0.1)\%$  for thermal neutrons for detectors incorporating a  $2.7\ \mu\text{m}$  thick of  $^{10}h\text{-BN}$  epilayer.

Since the uncertainty in neutron flux value is difficult to measure, we further verified the detection efficiency of  $^{10}h\text{-BN}$  detectors against a commercially certified  $^6\text{Li}$  filled microstructured Si semiconductor neutron detector (MSND) without needing to know the thermal neutron flux. The  $^6\text{Li}$  filled MSND is a Domino V4 neutron detector (model D411S-30-D0010-V4) from Radiation Detection Technologies Inc., which has a detection area of  $4\ \text{cm}^2$  and a specified absolute detection efficiency of 30% for thermal neutrons. By placing our  $^{10}h\text{-BN}$  detector and  $^6\text{Li}$  filled MSND at the same distance to the  $^{252}\text{Cf}$  source (9 cm away from the front surface of the HDPE moderator) and comparing the relative thermal neutron counts per unit area between our  $^{10}h\text{-BN}$  detector and  $^6\text{Li}$  filled MSND (with a known detection efficiency of 30%), we obtain a detection efficiency of  $\sim 4.1\%$

for  $^{10}\text{B}$ -BN detector, which is in excellent agreement with the value calculated from  $\eta = \frac{N_c}{N_{in}}$ . This agreement further ensures that both the specified value of neutron flux by Frontier Technology and the calculated value of thermal neutron flux irradiating on the detector,  $N_{in}$ , based on Monte Carlo N particle code simulations<sup>29</sup> are reliable.

The theoretical thermal neutron absorption length of 100% pure isotopically  $^{10}\text{B}$ -enriched  $^{10}\text{B}$ -BN is about 47  $\mu\text{m}$ , which is 5 times shorter than that of natural  $h$ -BN (237  $\mu\text{m}$ ), based on which the expected interaction probability of  $^{10}\text{B}$ -BN detectors (with a layer thickness of 2.7  $\mu\text{m}$ ) should be  $P \approx \frac{1}{\lambda} \times \frac{15}{18} = \frac{2.7}{47} \times \frac{15}{18} = 4.8\%$ . Here, the fraction  $\frac{15}{18}$  is included because the etched trench width is 3  $\mu\text{m}$  and so a fraction of  $\frac{3}{18}$  of the detection material was removed based on Fig. 6(a). The difference between the measured detection efficiency ( $\eta=4.0 (\pm 0.1)\%$ ) and the expected interaction probability ( $P=4.8\%$ ) can be accounted for by the charge collection efficiency ( $\eta_{coll}$ ) of  $^{10}\text{B}$ -BN detectors,  $\eta_{coll} = \frac{\eta}{P}$ , which is 83 ( $\pm 2$ )%. The charge collection efficiency ( $\eta_{coll}$ ) of  $^{10}\text{B}$ -BN detectors exceeds that of the natural  $h$ -BN detectors. Since both  $^{10}\text{B}$ -BN and natural  $h$ -BN have a comparable crystalline quality, the difference in  $\eta_{coll}$  suggests that dry etching potentially introduces defects which have an impact on the charge collection efficiency. The results indicate that although the MSM detector design with a micro-strip width of 15  $\mu\text{m}$  and etched trench width of 3  $\mu\text{m}$  shown in Fig. 6(a) adequately addresses the need of maximizing the detection area (minimizing the fraction of removed  $^{10}\text{B}$ -BN materials),  $\eta_{coll}$  can be further improved by implementing detector architectures which are doing away with dry etching.

#### IV. SUMMARY

In summary, natural and isotopically  $^{10}\text{B}$ -enriched  $h$ -BN epilayers with thicknesses of 4.5  $\mu\text{m}$  and 2.7  $\mu\text{m}$ , respectively, have been successfully synthesized by MOCVD. These materials were utilized to construct solid-state thermal neutron detectors. The results revealed that MSM detectors (with the micro-strip width of 15  $\mu\text{m}$  and etched trench width of 3  $\mu\text{m}$ ) incorporating isotopically  $^{10}\text{B}$ -enriched  $h$ -BN epilayers of 2.7  $\mu\text{m}$  in thickness exhibit an overall detection efficiency for thermal neutrons of 4% and a charge collection efficiency as high as 83%. Further material and device processing development will likely to produce  $h$ -BN detectors with improved performance and advance the charge collection efficiency to nearly 100%. Therefore, future efforts are to focus on the growth of  $h$ -BN epilayers with increased thicknesses to provide an enhanced interaction probability between thermal neutrons and  $h$ -BN and hence the overall detection efficiency. The ability to synthesis larger wafers of  $h$ -BN epilayers, the applicability of semiconductor processing technologies, and the outstanding attributes of high charge collection efficiency and high energy resolution of the reaction products of  $h$ -BN detectors, open up new opportunities to construct high sensitivity, compact, robust and low cost solid-state neutron detectors.

The efforts on  $h$ -BN material growth and neutron detector fabrication are supported by DHS ARI program (No. 2011-DN-077-ARI048) and the studies of the basic structural properties of  $h$ -BN epilayers are supported by NSF (ECCS-1402886). Jiang and Lin are grateful to the AT&T Foundation for the support of Ed Whitacre and Linda Whitacre endowed chairs.

- <sup>1</sup> Y. Kubota, K. Watanabe, O. Tsuda, and T. Taniguchi, *Science* **317**, 932 (2007).
- <sup>2</sup> K. Watanabe, T. Taniguchi, and H. Kanda, *Nat. Materials* **3**, 404 (2004).
- <sup>3</sup> K. Watanabe, T. Taniguchi, and H. Kanda, *Nat. Photonics* **3**, 591 (2009).
- <sup>4</sup> Y. Kobayashi, K. Kumakura, T. Akasaka, and T. Makimoto, *Nature* **484**, 223 (2012).
- <sup>5</sup> B. Arnaud, S. Lebègue, P. Rabiller, and M. Alouani, *Phys. Rev. Lett.* **96**, 026402 (2006).
- <sup>6</sup> R. Dahal, J. Li, S. Majety, B. N. Pantha, X. K. Cao, J. Y. Lin, and H. X. Jiang, *Appl. Phys. Lett.* **98**, 211110 (2011).
- <sup>7</sup> S. Majety, J. Li, X. K. Cao, R. Dahal, B. N. Pantha, J. Y. Lin, and H. X. Jiang, *Appl. Phys. Lett.* **100**, 061121 (2012).
- <sup>8</sup> A. K. Geim and I. V. Grigorieva, *Nature* **499**, 419 (2013).
- <sup>9</sup> G. F. Knoll, "Radiation detection and measurement," 4th ed. (John Wiley & Sons, 2010).
- <sup>10</sup> J. Li, R. Dahal, S. Majety, J. Y. Lin, and H. X. Jiang, *Nucl. Instr. Meth. Phys. Res. A* **654**, 417 (2011).
- <sup>11</sup> T. C. Doan, S. Majety, S. Grendadier, J. Li, J. Y. Lin, and H. X. Jiang, *Nucl. Instr. Meth. Phys. Res. A* **748**, 84 (2014).
- <sup>12</sup> T. C. Doan, S. Majety, S. Grendadier, J. Li, J. Y. Lin, and H. X. Jiang, *Nucl. Instr. Meth. Phys. Res. A* **783**, 121 (2015).
- <sup>13</sup> O. Osberghaus, *Zeitschrift fuer Physik* **128**, 366 (1950).
- <sup>14</sup> J. Uher, S. Pospisil, V. Linhart, and M. Schiebar, *Appl. Phys. Lett.* **90**, 124101 (2007).
- <sup>15</sup> M. A. Khan, J. N. Kuznia, R. A. Skogman, D. T. Olson, M. M. Millan, and W. J. Choyke, *Appl. Phys. Lett.* **61**, 2539 (1992).

- <sup>16</sup> J. Kim, S. Choi, D. Yoo, J. H. Ryou, R. D. Dupuis, R. F. Dalmau, P. Lu, and Z. Sitar, *Appl. Phys. Lett.* **93**, 022103 (2008).
- <sup>17</sup> H. X. Jiang and J. Y. Lin, *Semicon. Sci. Technol.* **29**, 084003 (2014).
- <sup>18</sup> S. Nakamura, G. Fasol, and S. J. Pearton, *The Blue Laser Diode: The Complete Story* (Springer, New York, 2000).
- <sup>19</sup> X. Z. Du, J. Li, J. Y. Lin, and H. X. Jiang, *Appl. Phys. Lett.* **106**, 021110 (2015).
- <sup>20</sup> S. J. Pearton, J. C. Zolper, R. J. Shul, and F. Ren, *J. Appl. Phys.* **86**, 1 (1999).
- <sup>21</sup> L. F. Voss, C. E. Reinhardt, R. T. Graff, A. M. Conway, R. J. Nikolic, N. Deo, and C. L. Cheung, *Nucl. Instr. Meth. Phys. Res. A* **606**, 821 (2009).
- <sup>22</sup> S. Grenadier, J. Li, J. Y. Lin, and H. X. Jiang, *J. Vac. Sci. Technol. A* **31**, 061517 (2013).
- <sup>23</sup> R. Dahal, K. C. Huang, J. Cliton, N. LiCausi, J.-Q. Lu, Y. Danon, and I. Bhat, *Appl. Phys. Lett.* **100**, 243507 (2012).
- <sup>24</sup> A. Many, *J. Phys. Chem. Solids* **26**, 575 (1965).
- <sup>25</sup> Y. Nemirovsky, A. Ruzin, G. Asa, and J. Gorelik, *J. Electronic Materials* **25**, 8 (1996).
- <sup>26</sup> P. R. Wallace, *Phys. Rev.* **71**, 622 (1947).
- <sup>27</sup> G. W. Semenoff, *Phys. Rev. Lett.* **53**, 2449 (1984).
- <sup>28</sup> X. K. Cao, B. Clubine, J. H. Edgar, J. Y. Lin, and H. X. Jiang, *Appl. Phys. Lett.* **103**, 191106 (2013).
- <sup>29</sup> J. Clinton, "Optimization and Characterization of a Novel Self Powered Solid State Neutron Detector," Doctoral Thesis, Rensselaer Polytechnic Institute), Chap. 3, 73–78 (2011).
- <sup>30</sup> R. C. Martin, J. B. Knauer, and P. A. Balo, *Appl Radiat Isot.* **53**, 785 (2000).
- <sup>31</sup> "Californium neutron sources & shipping containers for radioactive materials," Frontier Technology Corp. <http://www.frontier-cf252.com/index.html>.
- <sup>32</sup> F. P. Doty, US patent, 6727504.